Ultrasensitive interferometric on-chip microscopy of transparent objects

Roland A. Terborg,[1]* Josselin Pello,[1]* Ilaria Mannelli,[1] Juan P. Torres,[1,2] Valerio Pruneri[1,3]†

Light microscopes can detect objects through several physical processes, such as scattering, absorption, and reflection. In transparent objects, these mechanisms are often too weak, and interference effects are more suitable to observe the tiny refractive index variations that produce phase shifts. We propose an on-chip microscope design that exploits birefringence in an unconventional geometry. It makes use of two sheared and quasi-overlapped illuminating beams experiencing relative phase shifts when going through the object, and a complementary metal-oxide-semiconductor image sensor array to record the resulting interference pattern. Unlike conventional microscopes, the beams are unfocused, leading to a very large field of view (20 mm²) and detection volume (more than 0.5 cm³), at the expense of lateral resolution. The high axial sensitivity (<1 nm) achieved using a novel phase-shifting interferometric operation makes the proposed device ideal for examining transparent substrates and reading microarrays of biomarkers. This is demonstrated by detecting nanometer-thick surface modulations on glass and single and double protein layers.

INTRODUCTION

Since its invention, light microscopy has been evolving, and nowadays, a wide range of techniques is available to make "visible" what is "invisible." Many microscopes rely on changes in the illumination beam that are introduced by the sample to be measured and associated with optical effects, including light scattering, absorption, reflection, or their combination. When none of these physical mechanisms can produce any detectable signal, which is often the case with highly transparent objects such as biological cells and protein layers, one may still exploit phase shifts, that is, optical path differences (OPDs). This is the case, for example, with holographic (1–3) phase-contrast (4, 5) or differential interference contrast (DIC) (6) microscopy. Most of these microscopes, especially DIC, can offer high sensitivity and resolution. However, they also show a limited field of view (FOV) and depth of field (DOF) because light beams are focused onto the sample. One way to increase FOV and DOF is to use low–numerical aperture lenses or objectives, but this also reduces resolution and sensitivity and increases the device's size. For many applications, large FOV and DOF, and high axial sensitivity, are far more relevant than high lateral resolution.

Recently, an intense research effort has been devoted to developing lens-free microscopes (LFMs), which work in a scattering or holographic configuration and can offer unprecedented large DOF and FOV by using unfocused light beams and the full photosensitive area of a complementary metal-oxide semiconductor (CMOS) or a charge-coupled camera (7–15). For example, Oh et al. (13) and Mudanyali et al. (14) described an LFM in DIC configuration that detects very small objects but does not demonstrate large DOF nor high axial sensitivity. Here, we introduce a large-FOV interferometric on-chip microscope (LIM) based on a novel design and physical phase-shifting interferometry (PSI) that make it possible to achieve very high axial sensitivity and DOF. Compared to commercial DIC microscopes, the FOV (20 mm²) is

given by the CMOS image sensor array (ISA) is larger by at least two orders of magnitude, the axial sensitivity (OPD <1 nm) is similar, and the DOF (30 mm) is extended by three orders of magnitude at the expense of reducing lateral resolution (35 μm) (see fig. S1 for more details). We also show how the new scheme could measure nanometer-thick changes of the profile of a surface, mimicking, for example, defects or irregularities in transparent materials such as glass and polymers, and could also detect single and double protein layers. These initial demonstrations indicate the potential of the new platform, for example, in fast quality control of large-area glass substrates for displays or other consumer electronics products (16, 17), and the reading of microarray plates with a high number of biomarker targets (18–21).

RESULTS

The scheme is depicted in Fig. 1A, and a photograph of the newly designed LIM is shown in Fig. 1B. The LIM uses simple components: a CMOS ISA, two Savart plates (SPs; SP1 and SP2), one polarizer (P1), and one analyzer, which works as a second polarizer (P2). P1 is oriented at 45° in the transverse plane (xy) so that light entering SP1 contains an x-polarized beam (EPx) and a y-polarized beam (EPy) of equal amplitude. Each SP is composed of two birefringent crystals, which act differently on a light beam depending on its polarization (22). SP1 shears EPy with respect to EPx by a given distance s (in our case, 25 μm) in such a way that after exiting SP1, the two orthogonally polarized beams almost overlap and propagate in a parallel manner (Fig. 1C). Additional details on beam splitting, separation, and operation of the SPs, these being the key mechanisms and elements that allow the implementation of the new design, can be found in Materials and Methods. After the beams traverse the sample, SP2 exerts an equal and opposite shear (−s) with respect to SP1 so that, in the absence of any sample, the two recombined beams perfectly superimpose as if there was no polarization-dependent shearing of the beams. On the contrary, any refractive index change introduced by the sample that differently affects EPx and EPy will lead to a detectable OPD by transforming the

[1]ICFO-Institut de Ciències Fotòniques, The Barcelona Institute of Science and Technology, 08860 Castelldefels (Barcelona), Spain. [2]Department of Signal Theory and Communications, Universitat Politècnica de Catalunya, 08034 Barcelona, Spain. [3]ICREA-Institució Catalana de Recerca i Estudis Avançats, Passeig Lluís Companys 23, 08010 Barcelona, Spain.
*These authors contributed equally to this work.
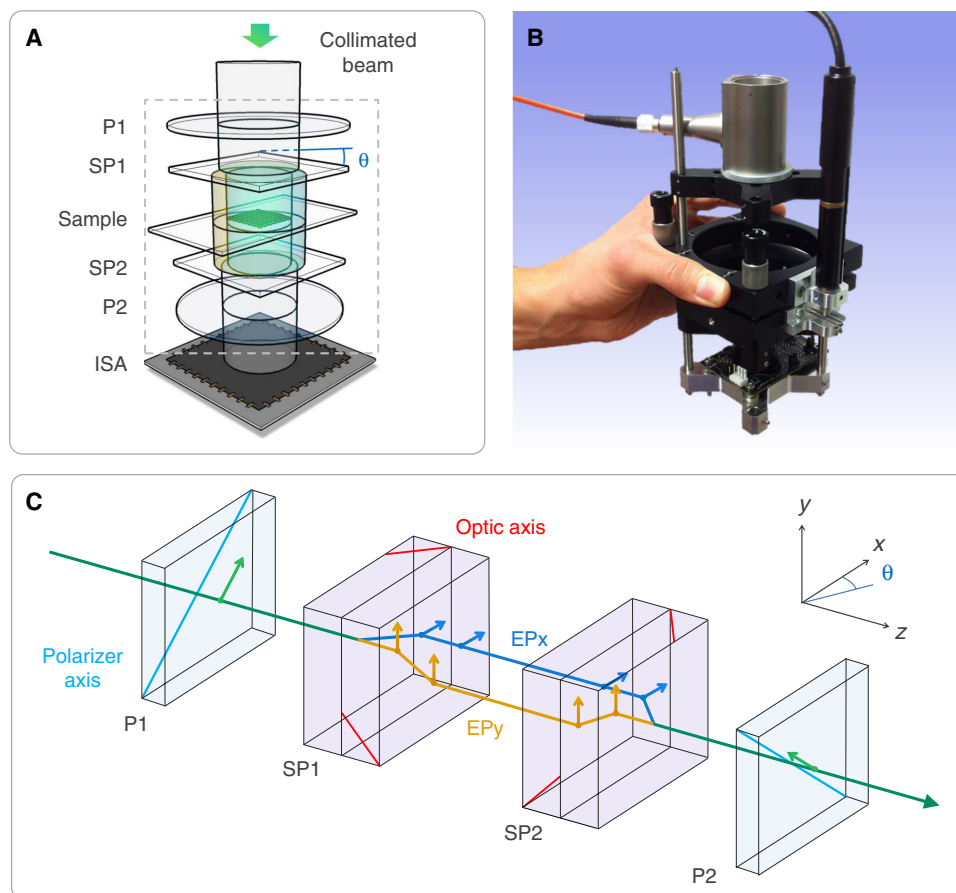†Corresponding author. Email: valerio.pruneri@icfo.eu

Fig. 1. LIM for ultrasensitive detection of transparent samples. (**A**) Scheme of the LIM. It comprises a light-emitting diode (LED) light source followed by a fiber collimator (not shown) generating a collimated beam, a polarizer (P1), two SPs (SP1 and SP2), the sample in between the SPs, an analyzer [that is, a second polarizer (P2) orthogonal to P1], and a CMOS ISA. (**B**) Photograph of the device. (**C**) Selection of the input polarization, splitting, shearing, and projection into an orthogonal direction in the LIM. Two SPs (SP1 and SP2) are placed between crossed polarizers (P1 and P2) to create a balanced Mach-Zehnder interferometer of partially overlapping and sheared beams (EPx and EPy) with orthogonal polarizations. Contrary to conventional DIC microscopes, no lenses are required to refocus EPx and EPy and make them interfere. This enables the achievement of high axial sensitivity over a large FOV.

resulting phase difference into intensity modulation using P2 that is orthogonal to P1. This creates an interferometric pattern over the full FOV of the camera revealed by the ISA (Fig. 2A, left). In contrast, no OPD modulation is detected in a noninterferometric configuration because of the complete transparency of the sample (Fig. 2A, right).

The sample in our scheme is in between two SPs. This means that the two interfering sheared beams (EPx and EPy) originated from the same beam, with the crucial advantage that any phase nonuniformities occurring outside the detection volume between the SPs are intrinsically compensated for. Furthermore, our design allows to continuously change the initial phase bias of the interferometer to operate in a PSI mode and, in this way, maximize the axial sensitivity of the system. This is achieved by tilting SP1, by means of a linear actuator, around the x or y axis within a range of 2° and with a resolution of about 2×10^{-5} degrees. By acquiring images at different SP1 tilts and applying the PSI method (23), we were able to enhance the detection of the interferometric signal present in the recorded images and measure OPDs on the order of $\lambda/1000$ (λ is the wavelength of the light). The workflow used to retrieve OPDs from images captured by the LIM is shown

in Fig. 2B. More details on the novel PSI scan, image capturing, and analysis can be found in Materials and Methods and the Supplementary Materials.

To demonstrate the potential for applications of the proposed technology, we measured three different transparent samples. For all these samples, we made sure that detection was related to phase shifts, that is, transversal spatial variations of OPD, which could only be read out interferometrically. This was confirmed by the fact that no patterns were observed for any sample when SPs or Ps were removed.

The first sample was a transparent indium tin oxide (ITO) ribbon (10 nm thick, 0.5 mm wide, and 7 mm long) deposited on a glass substrate (Fig. 3A). The ribbon produced a clear detected signal, which was dependent on the injected current. Because of the Joule and thermo-optic effects, the temperature and local refractive index of the ribbon and the glass beneath increased. Consequently, an increase in the detected image intensity was observed when increasing the injection current (see Fig. 3A). Using independent thermography measurements, we measured a maximum temperature of about 60°C with a lateral gradient across s of only 1°C (see the Supplementary
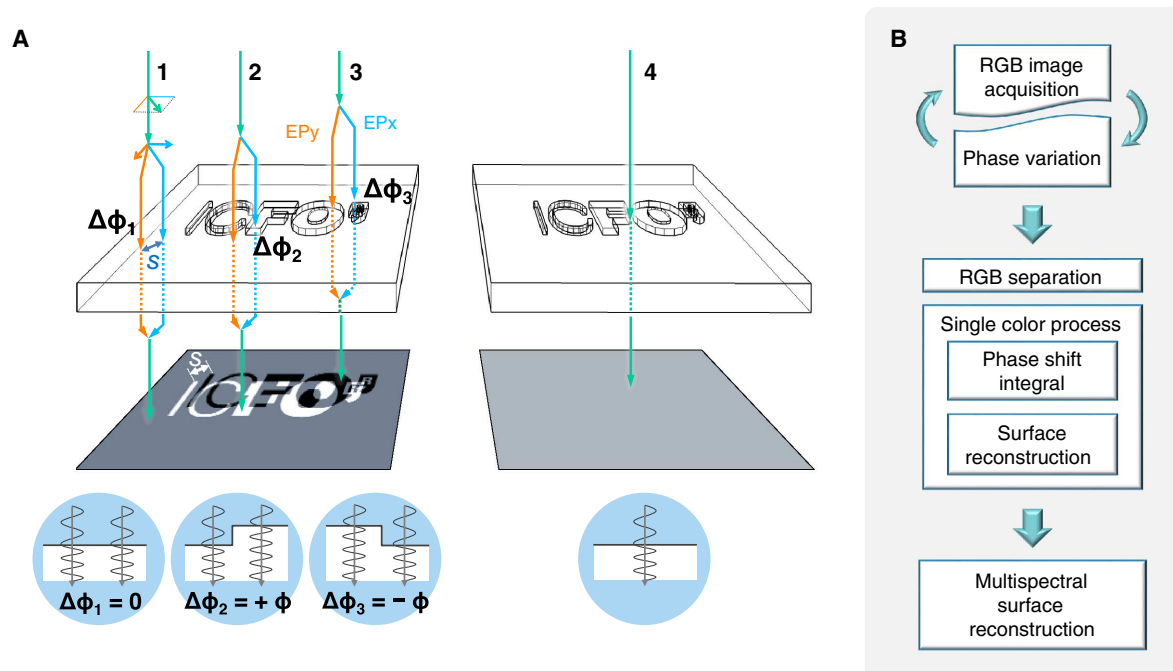
Fig. 2. Principle of detection of OPDs of transparent samples using the LIM. (A) Comparison between the LIM device (left scheme) and a non-interferometric setup (right). In the LIM, two orthogonally polarized beams (EPx and EPy) are symmetrically sheared by a distance s = 25 μm. Depending on the presence of spatially dependent relative phase shifts between them, an intensity pattern is detected on the ISA. By tilting SP1, an initial phase shift α between EPx and EPy can be introduced to maximize the sample detection. For instance, for $\alpha = \pi/2$, a relative phase-shift $\Delta\phi_1 = 0$ caused by the sample produces an intermediate intensity (gray zone), whereas $\Delta\phi_2 = +\phi$ and $\Delta\phi_3 = -\phi$ produce clearer (white) and darker (black) zones, respectively. In contrast, there is no formation of any image pattern when light (beam 4) propagates through a transparent sample in a noninterferometric configuration. **(B)** Workflow used to calculate the OPD maps.

Materials for calculations of the temperature distribution). Considering the value of the thermo-optic coefficient (1.2×10^{-5} K^{-1}) and thickness (1 mm) of the substrate, one could estimate the corresponding maximum detected OPD to be about 12 nm. In the calculation, we assumed the lateral temperature gradient to be constant through the whole thickness. Thus, the real OPD values were likely to be slightly smaller.

To gather more precise and quantitative data on the capability of the LIM, we measured a second set of samples of ultrathin silica (SiO$_2$) dot patterns on silica substrate (Fig. 3B). Two thicknesses were deposited by electron beam evaporation and measured for comparison by atomic force microscopy (AFM; d = 2 and 5 nm). The corresponding OPDs recovered from LIM imaging using the PSI method agreed with the AFM measurements. For example, the measured OPD of the thinnest sample was about 1 nm, which, considering the refractive index of silica (n = 1.45), corresponds to a physical thickness [OPD/(n – 1)] of the SiO$_2$ pattern of about 2.2 nm, in agreement with the AFM measurement (about 2 nm). A small area that makes the details of the SiO$_2$ pattern evident is shown in Fig. 3B. However, the images in our work always took over the full 20-mm^2 FOV of the ISA (see fig. S2).

The third sample consisted of protein layers deposited on a glass substrate. An array of monolayer spots of bovine serum albumin (BSA) was deposited on epoxysilane-coated glass (24) using a sciFLEX-ARRAYER S3 spotter (Scienion; see Fig. 3C). After incubation with anti-BSA immunoglobulin G (IgG), which specifically binds to BSA,

and rinsing, the BSA monolayer spots were converted to BSA + IgG bilayer spots. Imaging of both monolayer and bilayer arrays in the LIM resulted in their clear detection. The retrieved OPDs were 0.7 and 1.8 nm, respectively. For simplicity, we can assume that, after drying, each protein layer collapses in a dense layer of thickness proportional to the molecular weight of the protein. Because the molecular weights of BSA and IgG are 66 and 150 kD, respectively, if each BSA molecule had captured an IgG molecule, then the expected increase in OPD would have been 3.3 [~(150 + 66)/66], which is slightly higher than the observed value of 2.6 (~1.8/0.7). This suggested that most of the BSA proteins captured an IgG protein.

DISCUSSION

The proposed LIM design has several unique features. First, the opposite shears introduced respectively by SP1 and SP2 have the same effect on the optical path of the two beams EPx and EPy, thus ensuring a perfectly balanced interferometric configuration when no sample is present. This means that the LIM can work with a light source having a relatively short coherence length, with the advantage of strongly reducing detrimental effects such as standing wave patterns due to spurious reflections and speckle (25). The main constraint is that the coherence length should be larger than the OPDs to be detected. Because these are usually very small (less than 100 nm), incoherent light sources like LEDs become very suitable. In
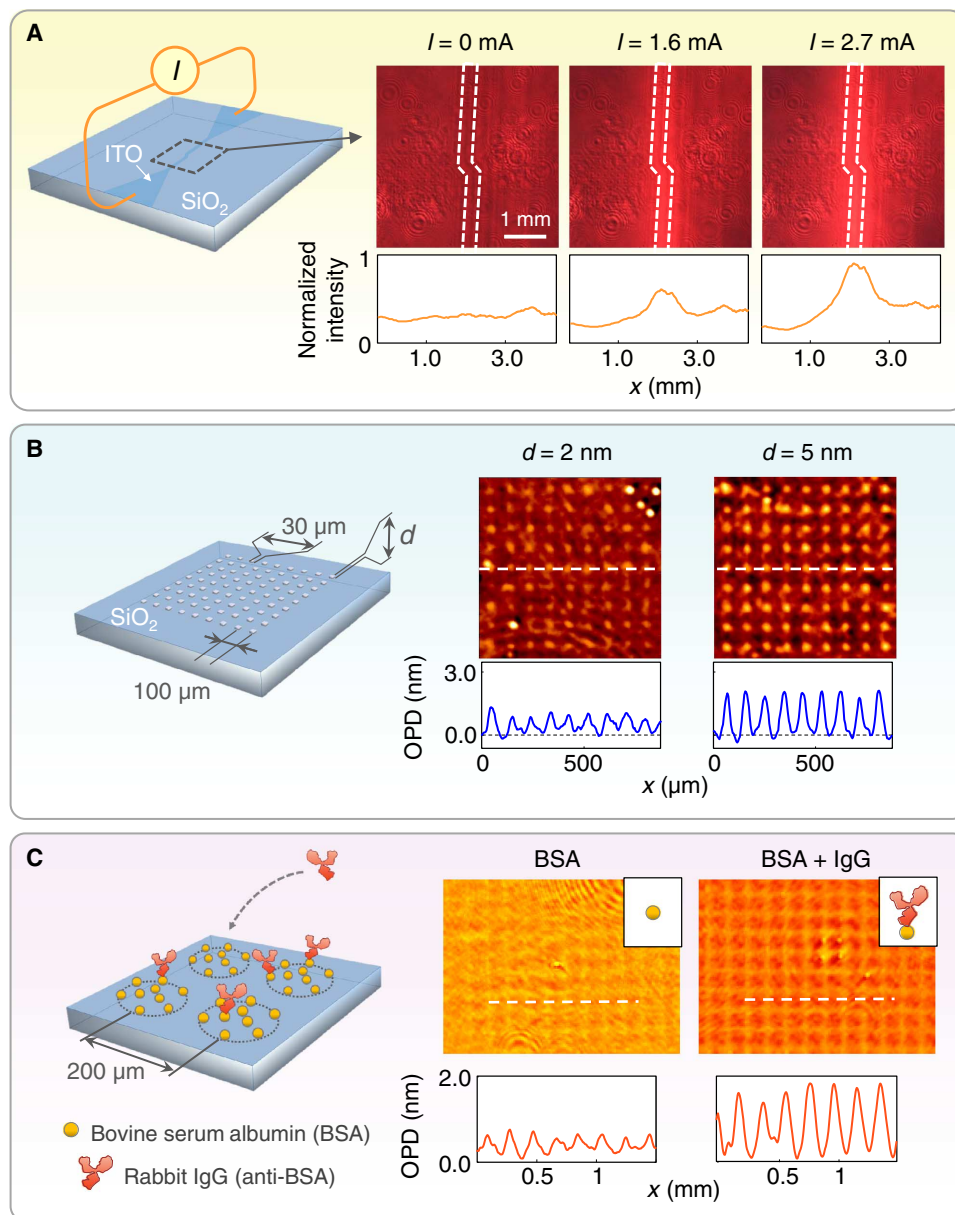
Fig. 3. Detection of transparent patterns using the proposed LIM. (A) An ITO ribbon on a silica (SiO_2) substrate is used to produce localized heating by injecting a constant current. The three images show refractive index (phase-shift) patterns induced through the thermo-optic effect, when injecting electric currents (I) of 0, 1.6, and 2.7 mA, respectively. The largest (steady-state) OPD detected is estimated to be 12 nm. **(B)** Silica dot patterns of different thicknesses (d) on a silica substrate are detected (spot diameter = 30 µm, pitch size = 100 µm). The measured OPD profiles (bottom graphs) agree with the thicknesses measured using AFM of 2 and 5 nm, respectively. **(C)** Detection of monolayer and bilayer protein arrays (spot diameter = 100 µm, array pitch = 200 µm). BSA monolayer spots after deposition on epoxysilane-coated glass and after incubation with anti-BSA IgG and rinsing. Both interferometric images and cross sections with OPD values are shown.

our experiments, the source was a multicolor LED system emitting at 465, 515, and 635 nm with a coherence length of 6 µm.

Secondly, each point of the EPx beam interferes with the corresponding sheared point of the EPy beam. This is an ideal situation for detecting periodic patterns with dimensions equal or larger than the shear distance s that makes the proposed LIM particularly effective in reading biomarker microarrays, which was shown above by detecting multiple spots of single and double protein layers. The shear distance s can be as small as the distance between two adjacent pixels, meaning that with the demonstrated configuration, more than 1 million biomarkers could be detected simultaneously by exploiting the full FOV.

Third, the small distance s between interfering points confers high stability to the device because potential mechanical and thermal fluctuations have similar effects on closely spaced regions and, thus, do not influence the relative OPD.

Fourth, contrary to microscopes that focus light, the FOV, DOF, and axial sensitivity are independent parameters, and the LIM has a DOF limited only by the physical space between the two SPs. This means that it can detect OPDs not only on the surface, as we did in the experiments, but also inside the volume of an object. In our experiments, this was demonstrated by placing the samples at various axial positions, up to 30 mm away from the ISA, and confirming that the quality of the detection (images) did not degrade appreciably. The experimental DOF of 30 mm was associated to a lateral resolution of 35 μm (see Image reconstruction in Material and Methods and fig. S2). Note that, if necessary, the lateral resolution can be significantly improved at the expense of DOF and detection volume.

Finally, the optomechanical alignment and assembly of the device are straightforward because the optical beam is of large dimensions and is not focused.

In conclusion, we have introduced and demonstrated a new on-chip interferometric microscope that combines DIC microscopy and LFM, with a novel PSI operation. Similarly to DIC, it allows detection of transparent samples with nanometric axial sensitivity and, at the same time, it provides large FOV and DOF, as do other LFMs. Besides optical performance, its simplicity and high optomechanical stability confer significant impact potential for a wide range of applications such as quality inspection of spatial patterns and defects in glass and polymer materials, in-line control of their fabrication processes, and label-free reading of large microarrays of multiple biomarkers. The new device is low-cost and compact, is already suitable for point-of-care applications, and may even become an accessory or be fully integrated in smart phones or tablets in the future.

MATERIALS AND METHODS

Savart plates
To split the beam coming from the light source into two orthogonally polarized beams, conventional DIC microscopes use a Wollaston prism (6). However, such a prism generates two orthogonally polarized beams that are not parallel, therefore requiring the use of lenses to alter the direction of propagation of the outgoing beams for making them interfere. Instead, the proposed LIM makes use of SPs that produce two nearly overlapping parallel and collimated beams. The selection of the polarization of the input beam by P1, the generation of two sheared beams with orthogonal polarizations in the two birefringent crystals composing the input SP, their recombination in the second SP, and the projection into a polarization orthogonal to input one by the output analyzer (polarizer) P2 are shown in Fig. 1C.

The optic axis of the first birefringent crystal of SP1 lies in the horizontal plane (xz). As a consequence, the vertically polarized beam (EPy) entering the crystal is an ordinary ray at normal incidence and does not experience refraction. Instead, the horizontally polarized beam (EPx) is not polarized perpendicularly to the optic axis; therefore, it experiences extraordinary refraction in the xz plane (26). Contrary to the first birefringent crystal, the optic axis of the second birefringent crystal of SP1 lies in the vertical plane (yz). Therefore, this time, EPx is an ordinary beam and propagates along z, whereas EPy experiences extraordinary refraction in the yz plane. After exiting SP1, EPx and EPy both propagate along z but are sheared by a distance s, which depends on the amount of birefringence and thickness of the

crystals used and on the wavelength of the light. In our experiments, the birefringent plates were made of quartz and had a thickness of 3 mm, and the optic axis was tilted at 45° with respect to the xy plane. The SPs composed of two such birefringent plates provided a shear of 25 μm.

Optical response of the LIM
Tilting the angle of incidence of the input beam incident onto the SP leads to a difference in OPD between the ordinary and extraordinary components (27–31). Following Eq. 1 in the study of Zhang et al. (28), if SP1 is tilted by a small angle (θ < 2°) around the y rotation axis, then the relative change in OPD (Δ_{OPD}) between the two orthogonally polarized components is proportional to θ

$$\Delta_{OPD} \propto t\left[\left(\frac{n_o^2 - n_e^2}{n_o^2 + n_e^2}\right)\theta\right] \tag{1}$$

where t is the thickness of the SP, and n_o and n_e are the ordinary and extraordinary refractive indices, respectively, of the birefringent crystals forming the SP.

Experimentally, we have confirmed that, for visible light, phase differences between the two components in the -2π to 2π range could be introduced without producing significant changes in beam separation (shear) or image displacement. The latter ones could not be detected because they always remain much smaller than our xy resolution limit. Similarly, we have assessed that Δ_{OPD} is linear with respect to small SP tilt angles (see fig. S3).

By tilting only one SP, the LIM becomes unbalanced, and its working point changes. For example, the quadrature condition (that is, $\Delta_{OPD}/\lambda = \pi/2 + m\pi$, with m being an integer) can be easily achieved. These points are characterized by a higher sensitivity to OPD changes, that is, a lower threshold for detection. This also allows us to access the full range of the response of the LIM.

To study the response of the LIM, for the sake of simplicity, we assumed uniform and monochromatic illumination at a given wavelength (λ), with polarization set by the first polarizer aligned along the $(\hat{x} + \hat{y})/\sqrt{2}$ axis. When a transparent sample is present, any nonuniformity will produce an OPD between the two orthogonally polarized beams. The electric field at an arbitrary point in the detection plane can be described as

$$\vec{E} = \frac{E_0}{\sqrt{2}} e^{i\beta}\left[e^{i(\alpha_x + \phi_x)}\hat{x} + e^{i(\alpha_y + \phi_y)}\hat{y}\right] \tag{2}$$

where β is an arbitrary initial phase for both polarizations, α_x and α_y are the phase differences experienced by the two orthogonally polarized beams due to the SP tilt, and ϕ_x and ϕ_y are the phase delays produced by the sample. After projection along the analyzer polarization (crossed polarization vector $(\hat{x} - \hat{y})/\sqrt{2}$), the amplitude of the signal becomes

$$E = \frac{E_0}{2} e^{i\beta}\left[e^{i(\alpha_x + \phi_x)} - e^{i(\alpha_y + \phi_y)}\right] \tag{3}$$

Assuming without a loss of generality that the SP tilt only affects the horizontal polarization, that is, $\alpha_x = \alpha$ and $\alpha_y = 0$ and writing $\phi_x - \phi_y = \phi$, it follows

$$E = E_0 e^{i\left(\beta + \frac{\alpha}{2} + \frac{\phi}{2}\right)} \sin\left(\frac{\alpha + \phi}{2}\right) \qquad (4)$$

This corresponds to light intensity

$$I(\alpha, \phi) = I_0 \sin^2\left(\frac{\alpha + \phi}{2}\right) \qquad (5)$$

Using the simple trigonometric equivalence $2\sin^2 x = 1 - \cos 2x$, the intensity becomes

$$I(\alpha, \phi) = \frac{I_0}{2}[1 - \cos(\alpha + \phi)] \qquad (6)$$

where $I_0 \propto |E_0|^2$

Phase-shifting interferometry method

In our device, we detected intensity patterns (interferometric images), and from these, we retrieved the sought-after spatially varying phase changes (OPDs) that characterize the transparent sample. Phase-shifting digital holography (PSDH) is a well-established technique (32) for processing images. It requires the detection of four holographic images (I_0, I_1, I_2, and I_3), which are generated by interfering the sample beam (containing the phase information to be retrieved) with a reference beam that can have one of four specific phase delays ($\alpha = \{0, \pi/2, \pi, 3\pi/2\}$) with respect to the sample beam. For a given sample's phase variation (ϕ), one obtains a set of intensities ($I(\alpha, \phi)$). According to PSDH theory, as described by Malacara (23), ϕ can be calculated as

$$\phi = \tan^{-1}\left[\frac{I(\pi/2, \phi) - I(3\pi/2, \phi)}{I(\pi, \phi) - I(0, \phi)}\right] \qquad (7)$$

However, in some applications, α cannot be precisely set. These experimental inaccuracies translate into errors in the detection of the phase. Moreover, when using multiple wavelengths (as in the case of multispectral imaging), a larger set of α phases is needed to have the specific phases for all wavelengths. Thus, it is more practical to use a broader set of interferograms (holograms) in the range $0 \leq \alpha \leq 2\pi$ and analyze them using a novel PSI method, which works as follows.

We defined the following weight functions

$$\Gamma_{\sin}(\alpha) = \frac{\sin\alpha}{\pi[n + m]} \qquad (8)$$

and

$$\Gamma_{\cos}(\alpha) = \frac{\cos\alpha}{\pi[n + m]} \qquad (9)$$

When integrating the different interferogram intensities with each weight function over a complete period of α, we obtained the PSI values

$$\Psi_{\sin} = \int_{-2m\pi}^{2n\pi} I(\alpha, \phi)\Gamma_{\sin}(\alpha)d\alpha = \frac{I_0}{2}\sin(\phi) \qquad (10)$$

and

$$\Psi_{\cos} = \int_{-2m\pi}^{2n\pi} I(\alpha, \phi)\Gamma_{\cos}(\alpha)d\alpha = -\frac{I_0}{2}\cos(\phi) \qquad (11)$$

From the PSI values, we then calculated both the phase and intensity as

$$\phi = -\tan^{-1}\left[\frac{\Psi_{\sin}}{\Psi_{\cos}}\right] \qquad (12)$$

$$I_0 = 2\sqrt{\Psi_{\sin}^2 + \Psi_{\cos}^2} \qquad (13)$$

By applying this measurement procedure with and without a sample, we subtracted signal noise, whose origin is illumination inhomogeneity, and other imperfections of the optical elements.

The high axial sensitivity images presented in this study were obtained using 20 tilt positions of SP1 covering the whole transfer function of the LIM (see fig. S3 for more details). The acquisition time was less than 6 s.

The processing time needed to extract the OPD from the raw images and reconstruct the high axial sensitivity image (see Image reconstruction) was around 2 min on a regular central processing unit (Intel Core i5). This processing time could be reduced at least five times, using previous knowledge of the tilting position at which each raw image was acquired and even further using parallelization or a graphics processing unit.

Image reconstruction

Because of the nature of the SPs, the phase information obtained with the PSI method is encoded as a duplicated (and shifted) image of the sample (see Fig. 2A). Furthermore, because the distance between the sample and the ISA (up to 30 mm in our experiments) is much larger than λ, the recorded pattern is diffracted with respect to the sample pattern. To retrieve the original optical path distribution, numerical image processing is required. This involves standard beam propagation and the use of a surface reconstruction program. To obtain the source image in a fast way, we used a Wiener deconvolution algorithm that considers that the point-spread function consists of two Dirac delta functions

$$PSF(x, y) = A\delta(x - s_x, y - s_y) + B\delta(x + s_x, y + s_y) \qquad (14)$$

where A and B are complex values, and s_x and s_y are the beam displacement components due to the SPs. Because the deconvolution might lead to dividing by 0 for some points, information from some regions, especially those near the zero frequency in the Fourier space, could be lost. An iterative method can be used to avoid the deconvolution algorithms (33).

SUPPLEMENTARY MATERIALS

Supplementary material for this article is available at http://advances.sciencemag.org/cgi/content/full/2/6/1600077/DC1

fig. S1. Comparison between a conventional DIC microscope and the proposed LIM in detecting transparent patterns (reading microarrays of biomarkers).

fig. S2. Lateral resolution of the LIM.

fig. S3. Measured transfer function of the LIM.

fig. S4. Simulation of the LIM response.

fig. S5. Heat distribution generated by an ITO ribbon deposited on a glass substrate.

Simulation of the LIM

Thermo-optic experiments

REFERENCES AND NOTES

1. D. Gabor, Microscopy by reconstructed wave-fronts. *Proc. R. Soc. A* **197**, 454–487 (1949).
2. R. F. Vanlingten, H. Osterberg, Holographic microscopy. *Nature* **211**, 282–283 (1966).
3. T. Zhang, I. Yamaguchi, Three-dimensional microscopy with phase-shifting digital holography. *Opt. Lett.* **23**, 1221–1223 (1998).
4. F. Zernike, Phase contrast, a new method for the microscopic observation of transparent objects. *Physica* **9**, 686–698 (1942).
5. S. Fürhapter, A. Jesacher, S. Bernet, M. Ritsch-Marte, Spiral phase contrast imaging in microscopy. *Opt. Express* **13**, 689–694 (2005).
6. R. D. Allen, G. B. David, G. Nomarski, The Zeiss-Nomarski differential interference equipment for transmitted-light microscopy. *Z. Wiss. Mikrosk.* **69**, 193–221 (1969).
7. A. Greenbaum, W. Luo, T.-W. Su, Z. Göröcs, L. Xue, S. O. Isikman, A. F. Coskun, O. Mudanyali, A. Ozcan, Imaging without lenses: Achievements and remaining challenges of wide-field on-chip microscopy. *Nat. Methods* **9**, 889–895 (2012).
8. L. Repetto, E. Piano, C. Pontiggia, Lensless digital holographic microscope with light-emitting diode illumination. *Opt. Lett.* **29**, 1132–1134 (2004).
9. X. Cui, L. M. Lee, X. Heng, W. Zhong, P. W. Sternberg, D. Psaltis, C. Yang, Lensless high-resolution on-chip optofluidic microscopes for *Caenorhabditis elegans* and cell imaging. *Proc. Natl. Acad. Sci. U.S.A.* **105**, 10670–10675 (2008).
10. S. O. Isikman, W. Bishara, S. Mavandadi, F. W. Yu, S. Feng, R. Lau, A. Ozcan, Lens-free optical tomographic microscope with a large imaging volume on a chip. *Proc. Natl. Acad. Sci. U.S.A.* **108**, 7296–7301 (2011).
11. O. Mudanyali, E. McLeod, W. Luo, A. Greenbaum, A. F. Coskun, Y. Hennequin, C. P. Allier, A. Ozcan, Wide-field optical detection of nanoparticles using on-chip microscopy and self-assembled nanolenses. *Nat. Photonics* **7**, 247–254 (2013).
12. A. E. Cetin, A. F. Coskun, B. C. Galarreta, M. Huang, D. Herman, A. Ozcan, H. Altug, Handheld high-throughput plasmonic biosensor using computational on-chip imaging. *Light Sci. Appl.* **3**, e122 (2014).
13. C. Oh, S. O. Isikman, B. Khademhosseinieh, A. Ozcan, On-chip differential interference contrast microscopy using lensless digital holography. *Opt. Express* **18**, 4717–4726 (2010).
14. O. Mudanyali, D. Tseng, C. Oh, S. O. Isikman, I. Sencan, W. Bishara, C. Oztoprak, S. Seo, B. Khademhosseinia, A. Ozcan, Compact, light-weight and cost-effective microscope based on lensless incoherent holography for telemedicine applications. *Lab Chip* **10**, 1417–1428 (2010).
15. J. M. Pérez, M. Jofre, P. Martínez, M. A. Yáñez, V. Catalan, V. Pruneri, An image cytometer based on angular spatial frequency processing and its validation for rapid detection and quantification of waterborne microorganisms. *Analyst* **140**, 7734–7741 (2015).
16. D. Lim, D.-H. Jeong, Zone-based inspection and defect classification for LCD manufacturing: Trivial defect free procedure for TFT glass inspection. *Int. J. Optomechatronics* **1**, 312–330 (2007).
17. H. Minami, J. Mori, S. Iwai, H. Moriya, N. Watanabe, Manufacturing and inspection equipment for efficient production of large LCDs. *Hitachi Rev.* **60**, 228–232 (2011).
18. G. MacBeath, Protein microarrays and proteomics. *Nat. Genet.* **32**, 526–532 (2002).
19. R. B. Jones, A. Gordus, J. A. Krall, G. MacBeath, A quantitative protein interaction network for the ErbB receptors using protein microarrays. *Nature* **439**, 168–174 (2006).
20. K. S. Anderson, S. Sibani, G. Wallstrom, J. Qiu, E. A. Mendoza, J. Raphael, E. Hainsworth, W. R. Montor, J. Wong, J. G. Park, N. Lokko, T. Logvinenko, N. Ramachandran, A. K. Godwin, J. Marks, P. Engstrom, J. LaBaer, Protein microarray signature of autoantibody biomarkers for the early detection of breast cancer. *J. Proteome Res.* **10**, 85–96 (2011).
21. X. Yu, J. LaBaer, High-throughput identification of proteins with AMPylation using self-assembled human protein (NAPPA) microarrays. *Nat. Protoc.* **10**, 756–767 (2015).
22. G. Barbarossa, Y. Zhou, Apparatus and method for optical interrogation. U.S. Patent 8,472,031 (2013).
23. D. Malacara, *Optical Shop Testing* (Wiley, Hoboken, NJ, ed. 3, 2007).
24. Y. Nam, D. W. Branch, B. C. Wheeler, Epoxy-silane linking of biomolecules is simple and effective for patterning neuronal cultures. *Biosens. Bioelectron.* **22**, 589–597 (2006).
25. J. W. Goodman, *Introduction to Fourier Optics* (McGraw-Hill, New York, 1968), 170 pp.
26. B. E. A. Saleh, M. C. Teich, *Fundamentals of Photonics* (Wiley, New York, ed. 2, 2007).
27. M. Françon, S. Mallick, *Polarization Interferometers: Applications in Microscopy and Macroscopy* (Wiley-Interscience, London, 1971).
28. C. Zhang, J. Zhao, Y. Sun, Influences of the thickness, misalignment, and dispersion of the Savart polariscope on the optical path difference and spectral resolution in the polarization interference imaging spectrometer. *Appl. Opt.* **50**, 3497–3504 (2011).
29. J. Li, J. Zhu, X. Hou, Comment on the paper "Design and analysis of wide-field-of-view polarization imaging spectrometer". *Opt. Eng.* **50**, 019702 (2011).
30. C. Zhang, T. Mu, Response to the comment on "Design and analysis of wide-field-of-view polarization imaging spectrometer". *Opt. Eng.* **50**, 049701 (2011).
31. M. Avendaño-Alejo, M. Rosete-Aguilar, Optical path difference in a plane-parallel uniaxial plate. *J. Opt. Soc. Am. A* **23**, 926–932 (2006).
32. I. Yamaguchi, T. Zhang, Phase-shifting digital holography. *Opt. Lett.* **22**, 1268–1270 (1997).
33. T. J. Holmes, W. J. Levy, Signal-processing characteristics of differential-interference-contrast microscopy. *Appl. Opt.* **26**, 3929–3939 (1987).